minerals

MDPI

Article

Gravity Data Enhancement Using the Exponential Transform of the Tilt Angle of the Horizontal Gradient

Luan Thanh Pham [1], Saulo Pomponet Oliveira [2], Cuong Van Anh Le [3], Nhung Thi Bui [4], An Hoa Vu [4] and Duong Anh Nguyen [4,*]

[1] Department of Geophysics, Faculty of Physics, University of Science, Vietnam National University, Hanoi 100000, Vietnam; luanpt@hus.edu.vn
[2] Graduate Program in Geology, Department of Mathematics, Federal University of Paraná, Curitiba 81531-980, PR, Brazil; saulopo@ufpr.br
[3] Department of Geophysics, Faculty of Physics and Engineering Physics, University of Science, Vietnam National University, Ho Chi Minh City 700000, Vietnam; lvacuong@hcmus.edu.vn
[4] Institute of Geophysics, Vietnam Academy of Science and Technology, Hanoi 100000, Vietnam; btnhung.vast@gmail.com (N.T.B.); hoanvt84@gmail.com (A.H.V.)
* Correspondence: naduong@igp.vast.vn

Abstract: Detecting the boundaries of geologic structures is one of the main tasks in interpreting gravity anomalies. Many methods based on the derivatives of gravity anomalies have been introduced to map the source boundaries. The drawbacks of traditional methods are that the estimated boundaries are divergent or false boundaries appear in the output map. Here, we use the exponential transform of the tilt angle of the horizontal gradient to improve the edge detection results. The robustness of the presented method is illustrated using synthetic data and real examples from the Voisey's Bay Ni-Cu-Co deposit (Canada) and the Tuan Giao (Vietnam). The findings show that the presented technique can produce more precise and clear boundaries.

Keywords: exponential transform; tilt angle; horizontal gradient; edge detection

check for updates

Citation: Pham, L.T.; Oliveira, S.P.; Le, C.V.A.; Bui, N.T.; Vu, A.H.; Nguyen, D.A. Gravity Data Enhancement Using the Exponential Transform of the Tilt Angle of the Horizontal Gradient. *Minerals* **2023**, *13*, 1539. https://doi.org/10.3390/min13121539

Academic Editors: Michael S. Zhdanov and Behnam Sadeghi

Received: 31 October 2023
Revised: 1 December 2023
Accepted: 6 December 2023
Published: 11 December 2023

1. Introduction

Geophysical methods are known as a powerful tool in mapping geological structures and minerals [1–6]. The gravity method is characterized by low cost and broad coverage compared to other geophysical surveys [7,8]. Interpreting gravity data provides important information about subsurface geological features [9–11]. The enhancement techniques of gravity anomalies can quickly determine the boundaries of the structures, and bring more abundant information for interpreting geologic formations [12–15].

Many techniques have been developed for enhancing gravity data [16–22]. These techniques are based on gradients of the anomalous field [23–26]. Unbalanced and balanced edge detection techniques are the two primary types of edge enhancement techniques [27]. The horizontal gradient [28], analytic signal [29], enhanced horizontal derivative [30], and analytic signals of gravity gradient tensor [31] are the unbalanced filters that are most often used for enhancing gravity data. The unbalanced methods can delineate the boundaries of shallow sources with high amplitudes, but they have limited detection effects on the boundaries of low amplitude anomalies [12,32].

To outline the boundaries of sources located at different depths, some balanced techniques have been developed. Most of these methods have been based on trigonometric functions, such as the tilt angle [33], theta map [34], exponential transform of the theta map [35], and normalized horizontal gradient [36]. A second generation of these methods involved high-order derivatives, for example, the tilt angle of the horizontal gradient [37], horizontal directional theta map [38], the horizontal gradient of the Ntilt [39], directional theta [40], logistic functions [41,42], enhanced horizontal gradient [43], and horizontal gradient of the improved normalized horizontal gradient [44]. The effectiveness of the edge detection techniques in terms of their precision in the determination of edges has been estimated in some recent studies [45–48]. Most of these studies showed that the tilt angle of the horizontal gradient is a powerful tool in mapping geological structures, but its edge map has a low resolution [46–48].

In this paper, we present a method to improve the edge detection results. Our method uses the exponential transform of the tilt angle of the horizontal gradient to bring the edge detection results with a high resolution and avoid producing additional edges in the output map. The application of the presented method is shown on real examples from the Voisey's Bay Ni-Cu-Co deposit (Canada) and the Tuan Giao (Vietnam).

2. Method

The theta map is a popular method in edge detection of potential field data, which normalizes the horizontal gradient by the analytic signal [34]. This method is defined as:

$$TM = cos\frac{\sqrt{\left(\frac{\partial F}{\partial x}\right)^2 + \left(\frac{\partial F}{\partial y}\right)^2}}{\sqrt{\left(\frac{\partial F}{\partial x}\right)^2 + \left(\frac{\partial F}{\partial y}\right)^2 + \left(\frac{\partial F}{\partial z}\right)^2}}. \quad (1)$$

where F is the gravity field.

To delineate the source boundaries more clearly, in 2013, Li suggested using the exponential transform of the theta map that is given by [35]:

$$ETM = exp\left(p \times cos\frac{\sqrt{\left(\frac{\partial F}{\partial x}\right)^2 + \left(\frac{\partial F}{\partial y}\right)^2}}{\sqrt{\left(\frac{\partial F}{\partial x}\right)^2 + \left(\frac{\partial F}{\partial y}\right)^2 + \left(\frac{\partial F}{\partial z}\right)^2}}\right). \quad (2)$$

where p is a constant decided by the interpreter. The use of p = 4 or 8 can make the edges more clearly [35]. The maxima of the *ETM* correspond to the source edges. Although the *ETM* can improve the resolution of the *TM*, it does not remove false edges in the edge map of the *TM*.

Another popular method is the tilt angle of the horizontal gradient that is given by [37]:

$$TAHG = atan\frac{\frac{\partial HG}{\partial z}}{\sqrt{\left(\frac{\partial HG}{\partial x}\right)^2 + \left(\frac{\partial HG}{\partial y}\right)^2}}. \quad (3)$$

where the horizontal gradient (HG) is given by:

$$HG = \sqrt{\left(\frac{\partial F}{\partial x}\right)^2 + \left(\frac{\partial F}{\partial y}\right)^2}. \quad (4)$$

Although the use of the *TAHG* can avoid bringing false information, its estimated boundaries are divergent. Here, we follow Li [35] to improve the resolution of the tilt angle of the horizontal gradient. The method is defined as:

$$ETAHG = exp\left(p \times atan\frac{\frac{\partial HG}{\partial z}}{\sqrt{\left(\frac{\partial HG}{\partial x}\right)^2 + \left(\frac{\partial HG}{\partial y}\right)^2}}\right). \quad (5)$$

The maxima of the *ETAHG* correspond to the source edges. Similar to the *TAHG*, it does not produce false information in the edge map. However, it can yield the edges with a higher resolution compared to the *TAHG*.

3. Methods Used for Comparison

To estimate the robustness of the presented method, we compared it to popular methods such as the horizontal gradient (*HG*), analytic signal amplitude (*AS*), theta map (*TM*), and some recent methods such as the exponential transform of the *TM* (*ETM*), tilt angle of the horizontal gradient (*TAHG*), horizontal gradient of *NTilt* (*HGNTilt*) and horizontal gradient of *impTDX* (*HGimpTDX*). The *HG*, *TM*, *ETM* and *TAHG* formulas are given in Section 2, while the *AS*, *HGNTilt* and *HGimpTDX* are shortly summarized below.

The *AS* is one of the most commonly used filters, which uses the peaks to extract the edges, and is defined as [29]:

$$AS = \sqrt{\left(\frac{\partial F}{\partial x}\right)^2 + \left(\frac{\partial F}{\partial y}\right)^2 + \left(\frac{\partial F}{\partial z}\right)^2}. \tag{6}$$

The *HGNTilt* uses the horizontal gradient of the *NTilt* to enhance the edges. The method is given by [39]:

$$HGNTilt = \sqrt{\left(\frac{\partial NTilt}{\partial x}\right)^2 + \left(\frac{\partial NTilt}{\partial y}\right)^2}, \tag{7}$$

where *NTilt* is defined as:

$$NTilt = atan\left(k^2 \frac{\frac{\partial^2 F}{\partial z^2}}{\sqrt{\left(\frac{\partial AS_2}{\partial x}\right)^2 + \left(\frac{\partial AS_2}{\partial y}\right)^2}}\right), \tag{8}$$

with AS_2 and k given by:

$$AS_2 = \sqrt{\left(\frac{\partial^3 F}{\partial z \partial z \partial x}\right)^2 + \left(\frac{\partial^3 F}{\partial z \partial z \partial y}\right)^2 + \left(\frac{\partial^3 F}{\partial z \partial z \partial z}\right)^2}, \tag{9}$$

$$k = \frac{M}{\sqrt{dx^2 + dy^2}}, \tag{10}$$

and M is the regional gravity value.

Recently, the *HGimpTDX* method was introduced to improve the resolution of the edges. The technique is based on the hyperbolic tangent function, and is given by [43]:

$$HGimpTDX = \sqrt{\left(\frac{\partial impTDX}{\partial x}\right)^2 + \left(\frac{\partial impTDX}{\partial y}\right)^2}, \tag{11}$$

where *impTDX* is defined as:

$$impTDX = tanh\frac{M\frac{\partial^2 F}{\partial z^2}}{\sqrt{\left(\frac{\partial TDX}{\partial x}\right)^2 + \left(\frac{\partial TDX}{\partial y}\right)^2}}. \tag{12}$$

with TDX given by [36]:

$$TDX = atan\frac{\sqrt{\left(\frac{\partial F}{\partial x}\right)^2 + \left(\frac{\partial F}{\partial y}\right)^2}}{\left|\frac{\partial F}{\partial z}\right|}. \quad (13)$$

4. Results and Discussion

4.1. Synthetic Examples

In this section, we estimate the effectiveness of the *ETAHG* through synthetic gravity examples with and without noise. The synthetic model includes five prisms, as shown in Figure 1a. The parameters of the model are presented in Table 1. Using these parameters, the gravity anomaly of the model is calculated and shown in Figure 1b.

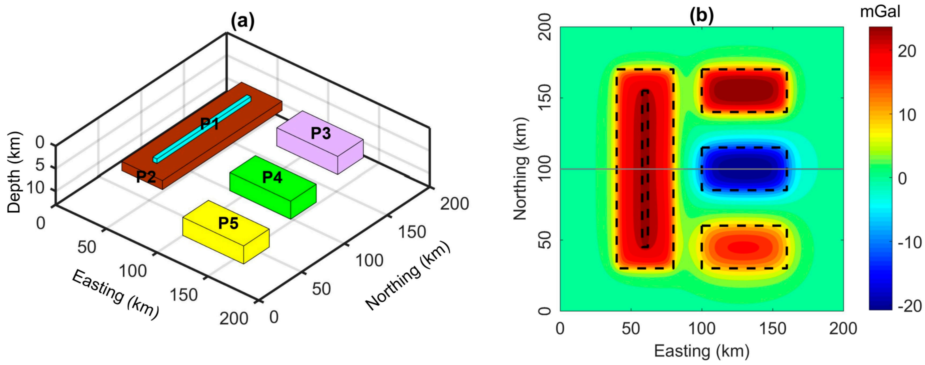

Figure 1. (**a**) The model. (**b**) Gravity anomaly of the model. The gray line denotes a profile.

Table 1. Parameters of the model.

Parameters	P1	P2	P3	P4	P5
Center coordinates (km; km)	60; 100	60; 100	130; 155	130; 100	130; 45
Width (km)	4	40	30	30	30
Length (km)	110	140	60	60	60
Depth of top (km)	2	3	3	6	9
Depth of bottom (km)	3	5	7	10	13
Density contrast (g/cm^3)	0.2	0.3	0.2	−0.2	0.2

In the first example, we applied the selected methods to gravity data in Figure 1b. Figure 2a presents the result of the *HG* method. It can be observed that the *HG* cannot equalize the different anomalies. The *HG* can determine the edges of the sources P2 and P3, but responses from other sources are faint. Figure 2b displays the edges outlined by the *AS*. It is observed that the *AS* is less effective in mapping the edges of the thin or deep sources. The results obtained from the method are fairly faint. Figure 2c presents the edges determined by the *TM* method. The method can equalize anomalies with different amplitudes, but it generates some false edges around the body P4. Figure 2c displays the edges determined by the *ETM* with p = 1. It is obvious that the *ETM* result is similar to the *TM* but has a higher resolution. The *ETM* was also computed using p = 4 (Figure 2e) and 8 (Figure 2f), as recommended in [35]. Clearly, the use of the *ETM* with p = 8 can generate sharper signals over the edges but the edge information of the body P1 is lost. Figure 2g,f display the edges delineated by the *HGNTilt* and *HGimpTDX* methods, respectively. Both methods generate the edges with a very high resolution, but some additional edges appear in the output maps of these methods. Figure 2i presents the edges determined by the *TAHG* method. Although the method can detect all the edges, the edges obtained from this method are divergent. Figure 2j–o display the edges delineated by the *ETAHG* with p = 1, 2, 3, 4, 6 and 8, respectively. As can be observed from these figures, the *ETAHG* maps have a higher resolution compared to the *TAHG*. Although the resolution of the *ETAHG* map increases when using larger values of p, the edges of the body P1 are lost or faint.

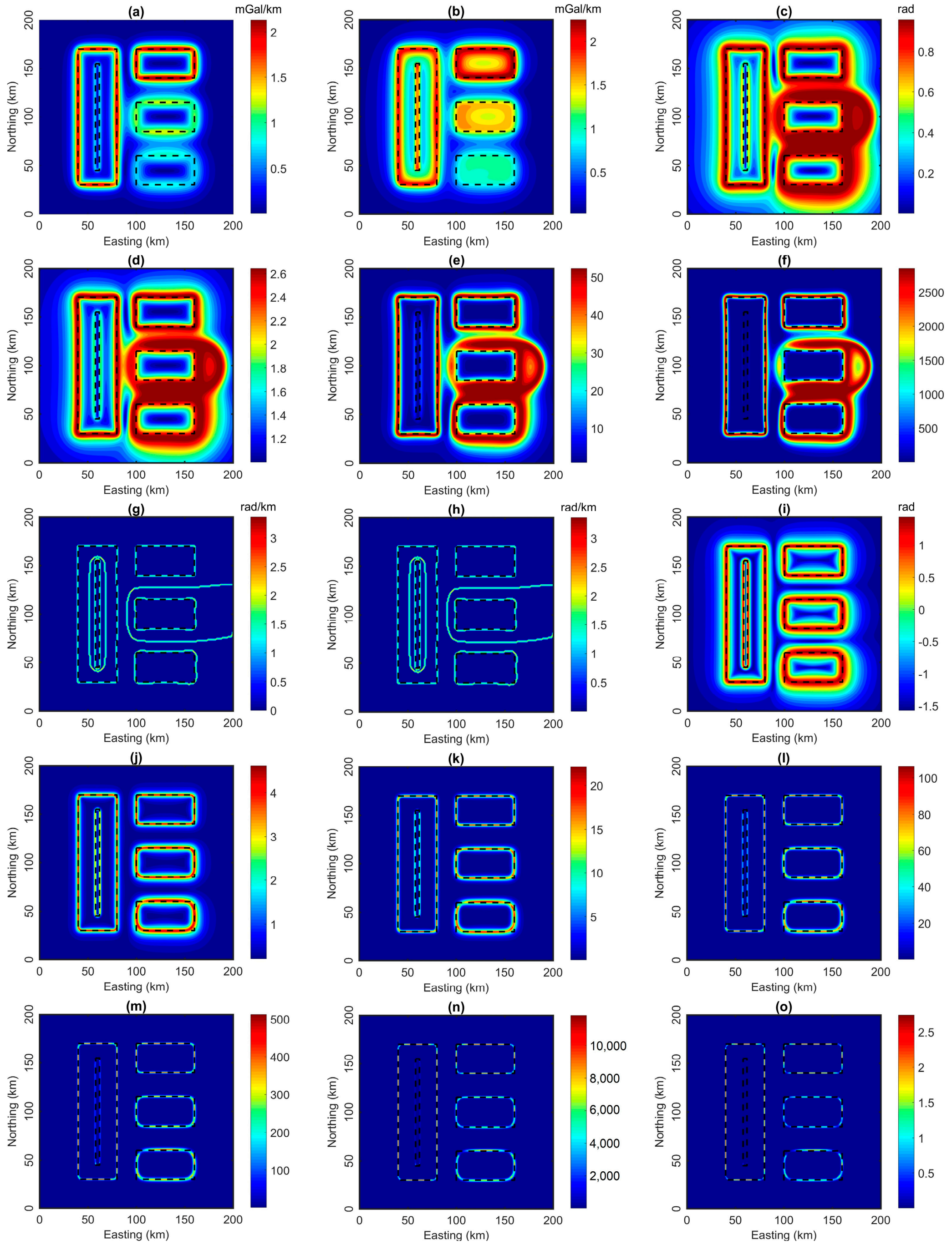

Figure 2. Results of data in Figure 1b. (**a**) *HG*. (**b**) *AS*. (**c**) *TM*. (**d**) *ETM* with $p = 1$. (**e**) *ETM* with $p = 4$. (**f**) *ETM* with $p = 8$. (**g**) *HGNTilt*. (**h**) *HGimpTDX*. (**i**) *TAHG*. (**j**) *ETAHG* with $p = 1$. (**k**) *ETAHG* with $p = 2$. (**l**) *ETAHG* with $p = 3$. (**m**) *ETAHG* with $p = 4$. (**n**) *ETAHG* with $p = 6$. (**o**) *ETAHG* with $p = 8$.

The results of the *TAHG* and *ETAHG* from Figure 2 were also compared in a horizontal profile (Figure 1b). Figure 3a shows the gravity anomaly along this profile. Figure 3b–h display the edges determined by the *TAHG* and *ETAHG* with p = 1, 2, 3, 4, 6 and 8, respectively. One can note from these figures that the signals over the edges along the *ETAHG* profiles are sharper than those of the *TAHG*. However, the amplitude of the transformed signal over the source P1 decreases as the p value increases. The *ETAHG* produces weak amplitude responses when the p value is greater than or equal to 2. For this reason, we used $p = 1$ in the subsequent *ETAHG* calculations.

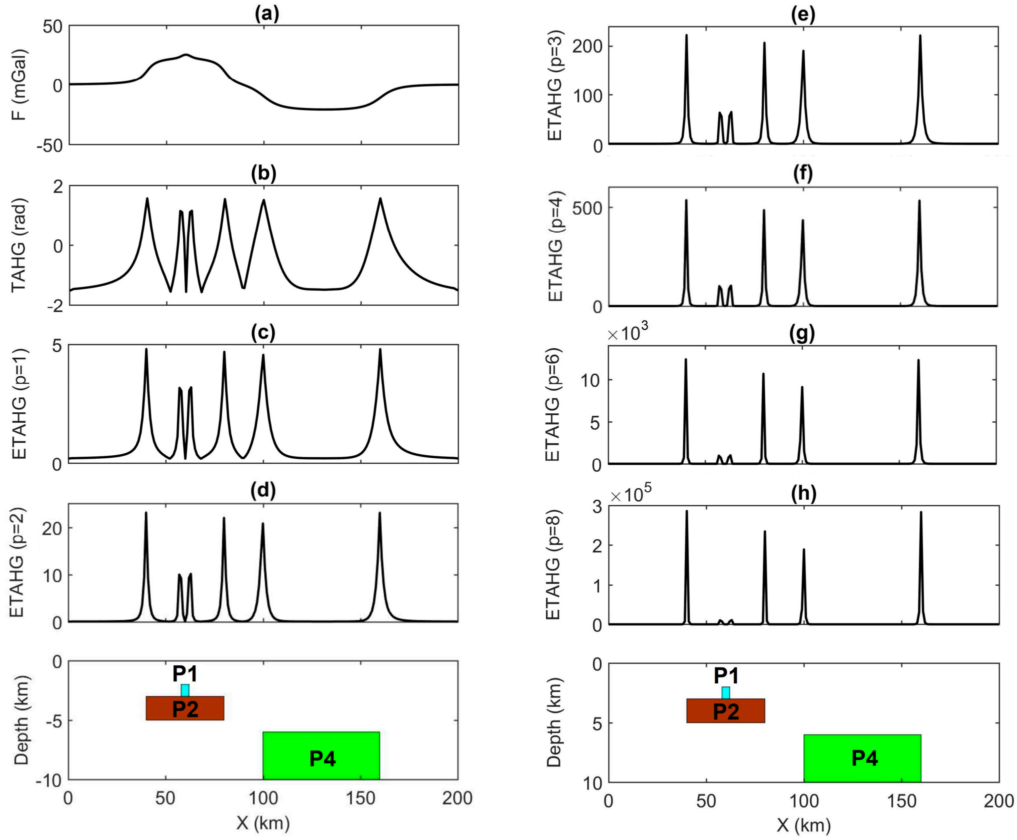

Figure 3. (**a**) Gravity data along the profile in Figure 1b. (**b**) *TAHG*. (**c**) *ETAHG* with $p = 1$. (**d**) *ETAHG* with $p = 2$. (**e**) *ETAHG* with $p = 3$. (**f**) *ETAHG* with $p = 4$. (**g**) *ETAHG* with $p = 6$. (**h**) *ETAHG* with $p = 8$.

To estimate the sensitivity of the *ETAHG* to random noise, we consider the second example where gravity data in Figure 2b was corrupted with 3% Gaussian noise (Figure 4a). Figure 5a–h display the edges delineated by applying the *HG*, *AS*, *TM*, *ETM*, *HGNTilt*, *HGimpTDX*, *TAHG* and *ETAHG* to gravity data in Figure 4a, respectively. As can be observed from these figures, the *HG* and *AS* are less sensitive to noise than others. However, these methods are dominated by the bodies P2 and P3. The *TM*, *ETM*, *HGNTilt*, *HGimpTDX*, *TAHG* and *ETAHG* are less sensitive to the depth of the bodies. As the *HGNTilt* and *HGimpTDX* are based on the third derivatives and/or fourth derivatives, they are more sensitive to noise than the *TM*, *ETM*, *TAHG* and *ETAHG*. In this case, the *ETAHG* still shows the edges more clearly than other methods.

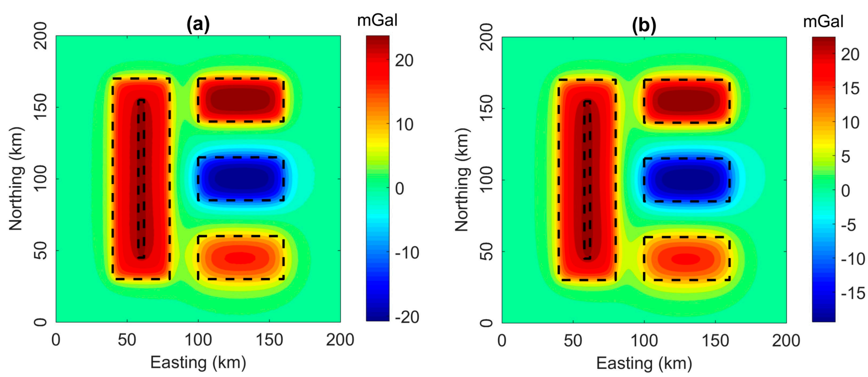

Figure 4. (**a**) Gravity data corrupted with 3% Gaussian noise. (**b**) Upward continued gravity data.

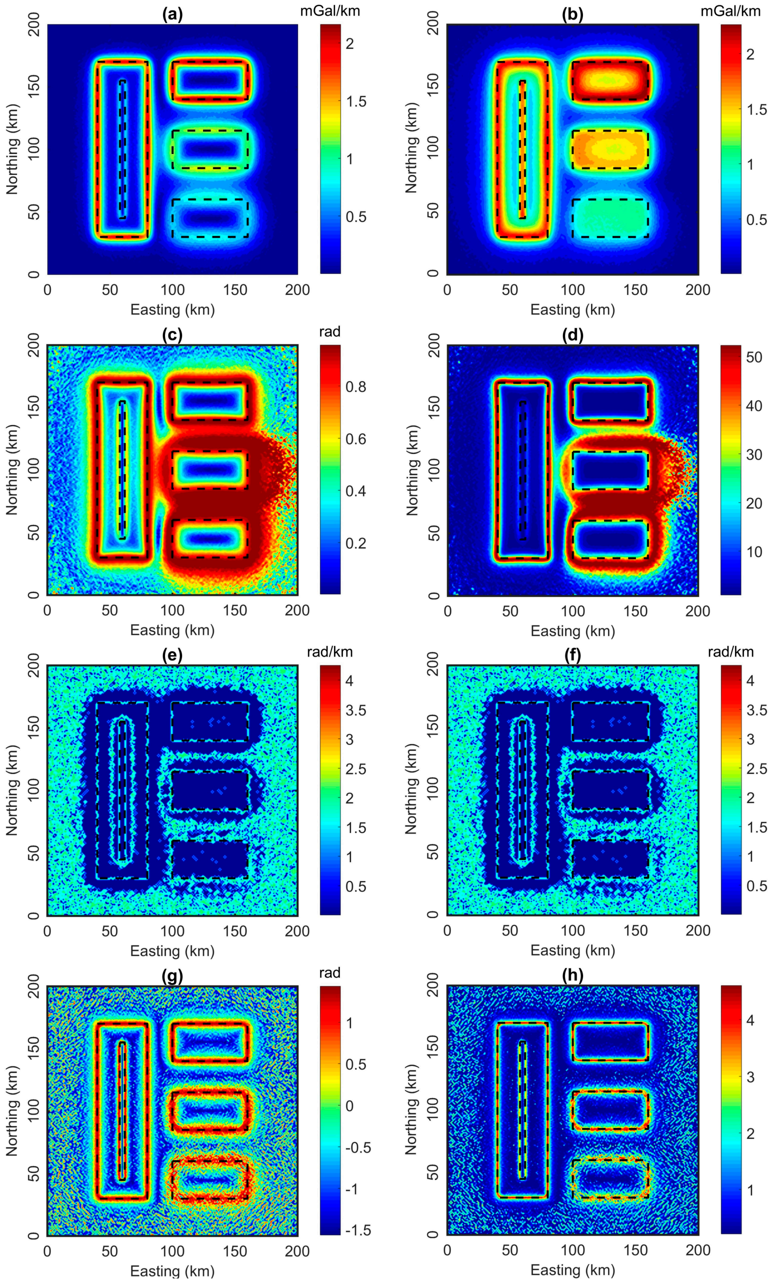

Figure 5. Results of data in Figure 4a. (**a**) *HG*. (**b**) *AS*. (**c**) *TM*. (**d**) *ETM* with p = 4. (**e**) *HGNTilt*. (**f**) *HGimpTDX*. (**g**) *TAHG*. (**h**) *ETAHG* with p = 1.

Since the enhancement techniques of gravity data are based on derivatives of the field, they amplify the noise. To attenuate the noise effect, the noise-corrupted data were subjected to an upward continuation filter of 1 km before using the techniques (Figure 4b). Figure 6a–h present the edges delineated by applying the *HG*, *AS*, *TM*, *ETM*, *HGNTilt*, *HGimpTDX*, *TAHG* and *ETAHG* to gravity data in Figure 4b, respectively. It is obvious that the *HG* can clearly outline the edges of the bodies P2 and P3, but the responses over the other sources are faint (Figure 6a). The *AS* cannot outline the edges of the dike P1 and deep sources P4 and P5 (Figure 6b). The *ETM* shows sharper edges than the *TM*, but both methods still generate false boundaries around the body P4 (Figure 6c,d). Although the *HGNTilt* and *HGimpTDX* can determine most of the edges with a very high resolution, some additional edges still appear along the north-south edges of the body G1, and around the body P4 output maps of these methods (Figure 6e,f). The *TAHG* and *ETAHG* can highlight all the source boundaries without any false information. However, the *ETAHG* generates higher resolution boundaries of the sources.

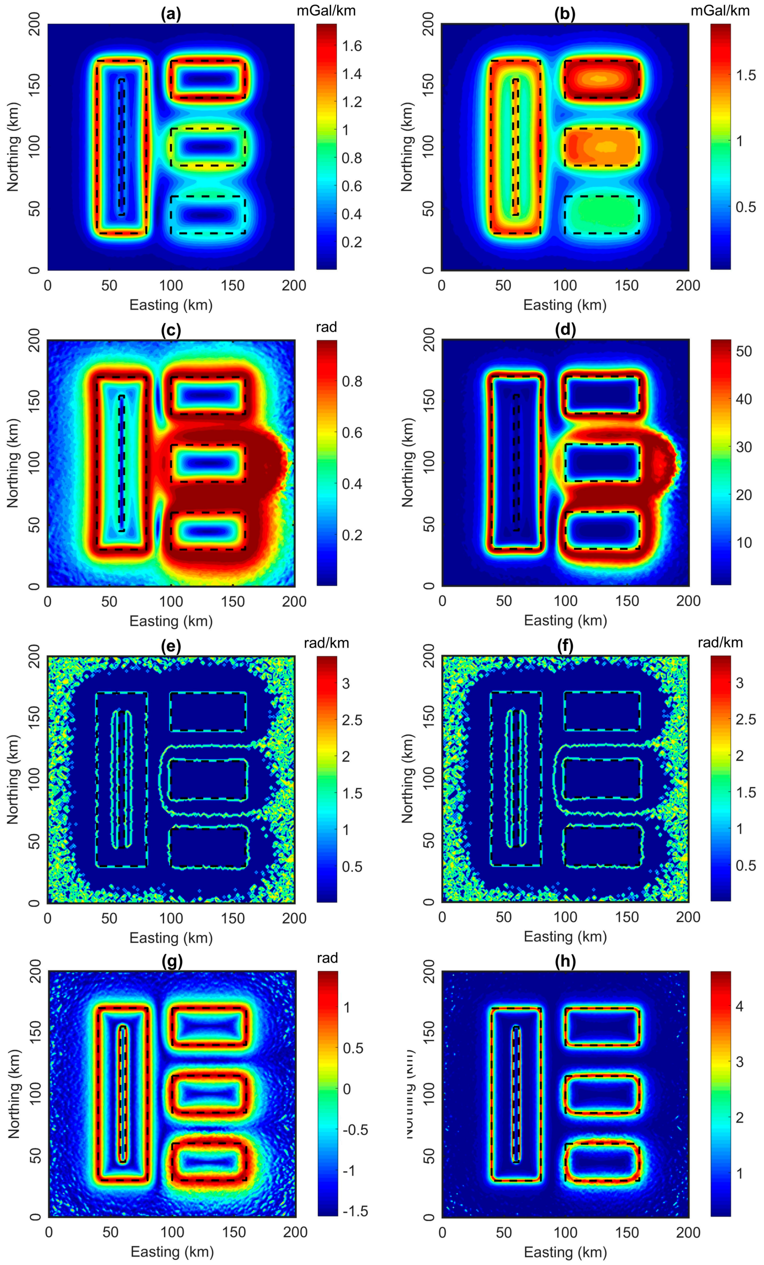

Figure 6. Results of data in Figure 4b. (**a**) *HG*. (**b**) AS. (**c**) *TM*. (**d**) *ETM* with *p* = 4. (**e**) *HGNTilt*. (**f**) *HGimpTDX*. (**g**) *TAHG*. (**h**) *ETAHG* with *p* = 1.

4.2. Real Examples

4.2.1. Voisey's Bay Ni-Cu-Co Deposit

One of the most important mineral discoveries in Canada over the last few decades is the Voisey's Bay Ni–Cu–Co deposit, which is situated on the northeast coast of Labrador (Figure 7) [49]. The primary ore body is the ovoid that is being mined at the moment (Figure 7). With horizontal dimensions of 650 by 350 m and a maximum depth extension of 120 m, it is a massive sulphide lens with an elliptical shape. It is estimated that there are 30 million tons of proven and probable reserves, grading 2.9% nickel, 1.7% copper, and 0.14% cobalt [49]. The deposit is linked to the Voisey's Bay intrusion, which crosses the 1.85 Ga east-dipping collisional boundary between the Archean Nain Province to the east and the Proterozoic Churchill Province to the west (Figure 7) [50,51].

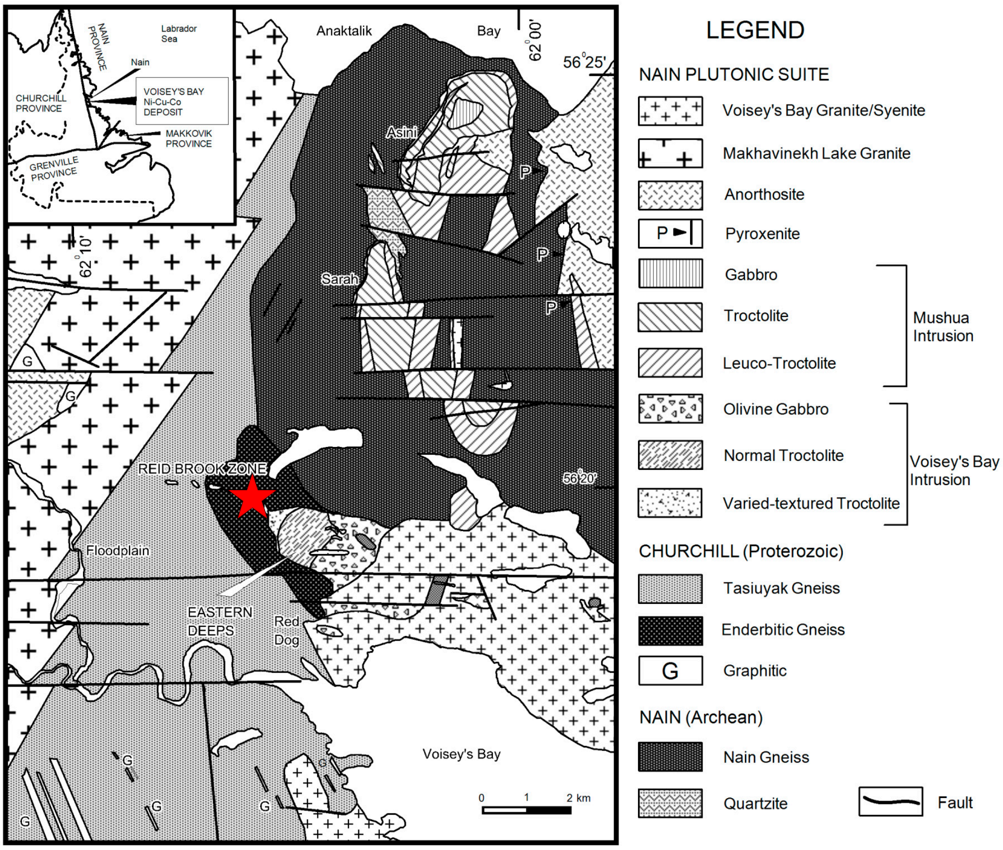

Figure 7. Geology of the Voisey's Bay area showing the location of the Voisey's Bay Ni-Cu-Co deposit (red star) (adapted from [50,51]).

The Bouguer gravity map of the Voisey's Bay is shown in Figure 8a [52]. The Bouguer gravity map of the Voisey's Bay comprises the primary ore body. Figure 8b–i present the edges delineated by applying the *HG*, *AS*, *TM*, *ETM*, *HGNTilt*, *HGimpTDX*, *TAHG* and *ETAHG* to gravity data in Figure 8a, respectively. It can be observed that the peaks of the *HG*, *HGNTilt*, *HGimpTDX*, *TAHG* and *ETAHG* demonstrated the presence of a primary ore body with an approximate ellipsoidal form, as reported by some other studies (Figure 8b,f–i) [49,53]. However, the *HG* and *TAHG* results are divergent. The *HGNTilt* and *HGimpTDX* are very effective in providing high resolution boundaries, but they bring some additional boundaries at the edges of the study area. In this case, the *AS* does not provide a clear image of the main ore body (Figure 8c), while the *TM* and *ETM* bring false maxima in the northeastern region. Comparing the results, one can observe that the *ETAHG* does not yield additional edges, and it can provide the edges more clearly compared to others.

4.2.2. Tuan Giao Area

The Tuan Giao area is located between the South China block and the Sundaland block. It is considered as a part of the transition boundary zone between these two blocks [54]. Two main factors, the (i) collision of the Indo-Australian and Eurasian plates and (ii) subduction of the Pacific plate under Eurasian plate, explain that the Tuan Giao area has high dynamic activities. The Tuan Giao is a mountainous area with a complicated geological structure (Figure 9), dominated by many active faults, such as the Dien Bien Phu fault, Son La fault, Song Da fault and Song Ma fault [55–57]. From the works of many researchers, young materials (i.e., magmatic rocks) intruded into old sedimentary rocks environment through the faults (Figure 9) [55,56]. For this area, Permian–Triassic sediment rocks dominate the most area while the rest as thin stripes disseminate along faults. In this area, there were at least seven earthquakes, with a magnitude of above five occurring from 1914 to 1983. These earthquakes are shown in Figure 5. The two biggest earthquakes occurred at Dien Bien in

1935 (M 6.8) and Tuan Giao in 1983 (M 6.7) (Figure 9). Both earthquakes severely damaged homes and infrastructure and killed or injured dozens of people in landslides [54]. Since then, no earthquakes with a magnitude of 5 have occurred in the study area; thus, this is a high-risk area for earthquakes. Therefore, accurately determining the location of faults in high-risk earthquake areas is necessary to have accurate earthquake hazard assessments and earthquake forecasts in the area.

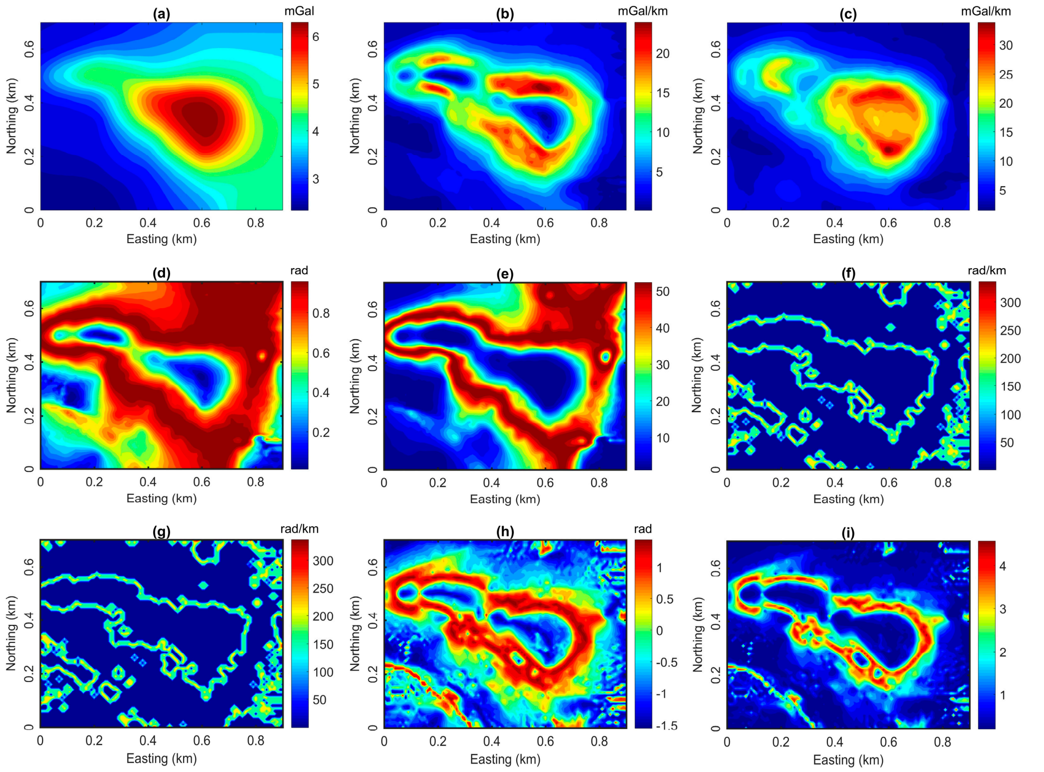

Figure 8. (**a**) Bouguer data of the Voisey's Bay Ni–Cu–Co deposit. (**b**) *HG*. (**c**) *AS*. (**d**) *TM*. (**e**) *ETM* with $p = 4$. (**f**) *HGNTilt*. (**g**) *HGimpTDX*. (**h**) *TAHG*. (**i**) *ETAHG* with $p = 1$.

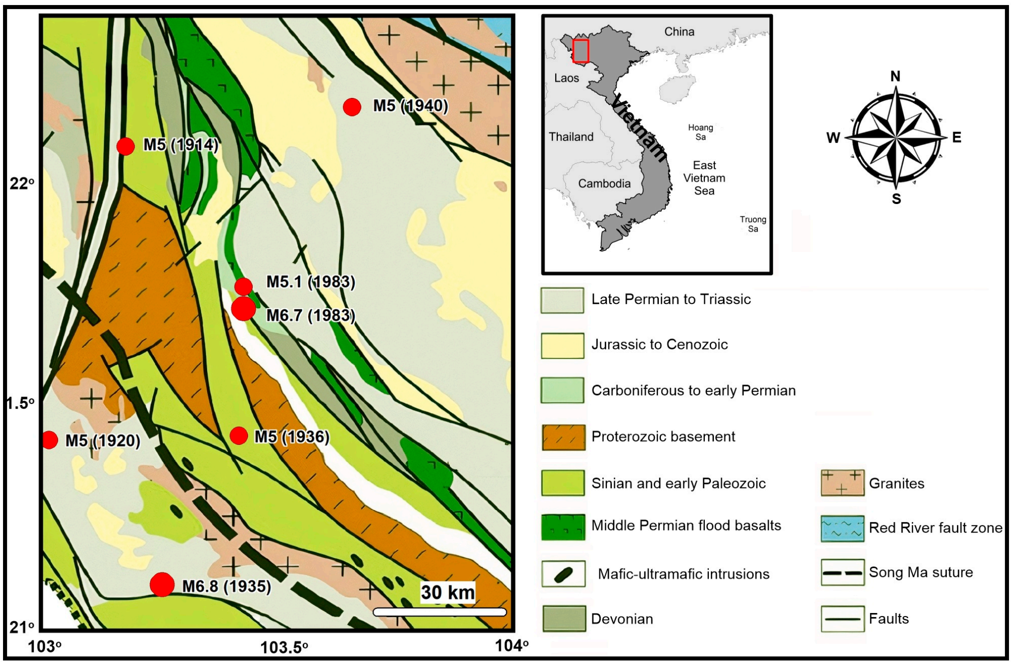

Figure 9. Geology map of the Tuan Giao [55].

Figure 10a displays the Bouguer gravity map of the Tuan Giao [58]. Figure 10b–i display the boundaries delineated by applying the *HG*, *AS*, *TM*, *ETM*, *HGNTilt*, *HGimpTDX*, *TAHG* and *ETAHG* to Bouguer gravity data in Figure 10a, respectively. One can observe that the *HG* and *AS* are dominated by anomalies at the northern part of the area, and these methods do not yield images of the structural boundaries. The obtained image maps from the application of the *TM*, *ETM*, *HGNTilt*, *HGimpTDX* and *TAHG* allow us to extract the structural boundaries, and show the boundaries of the large and small signals clearly (Figure 10d–h). While the edges in the *TM*, *ETM* and *TAHG* are divergent, the *HGNTilt* and *HGimpTDX* produce very sharp edges. However, the use of the *HGNTilt* and *HGimpTDX* may bring some additional edges, as shown in the synthetic examples. In this case, the edges determined by the *ETAHG* are more precise and clearer (Figure 10i). It can be observed from Figure 10i that the *ETAHG* map shows a dominant NW-SE structural trend of density bodies that correspond favorably to the geological formations of the Tuan Giao. In addition, the maximum locations in the *ETAHG* map exhibit a strong correlation with a large number of NW-NW-SE trending faults in the region.

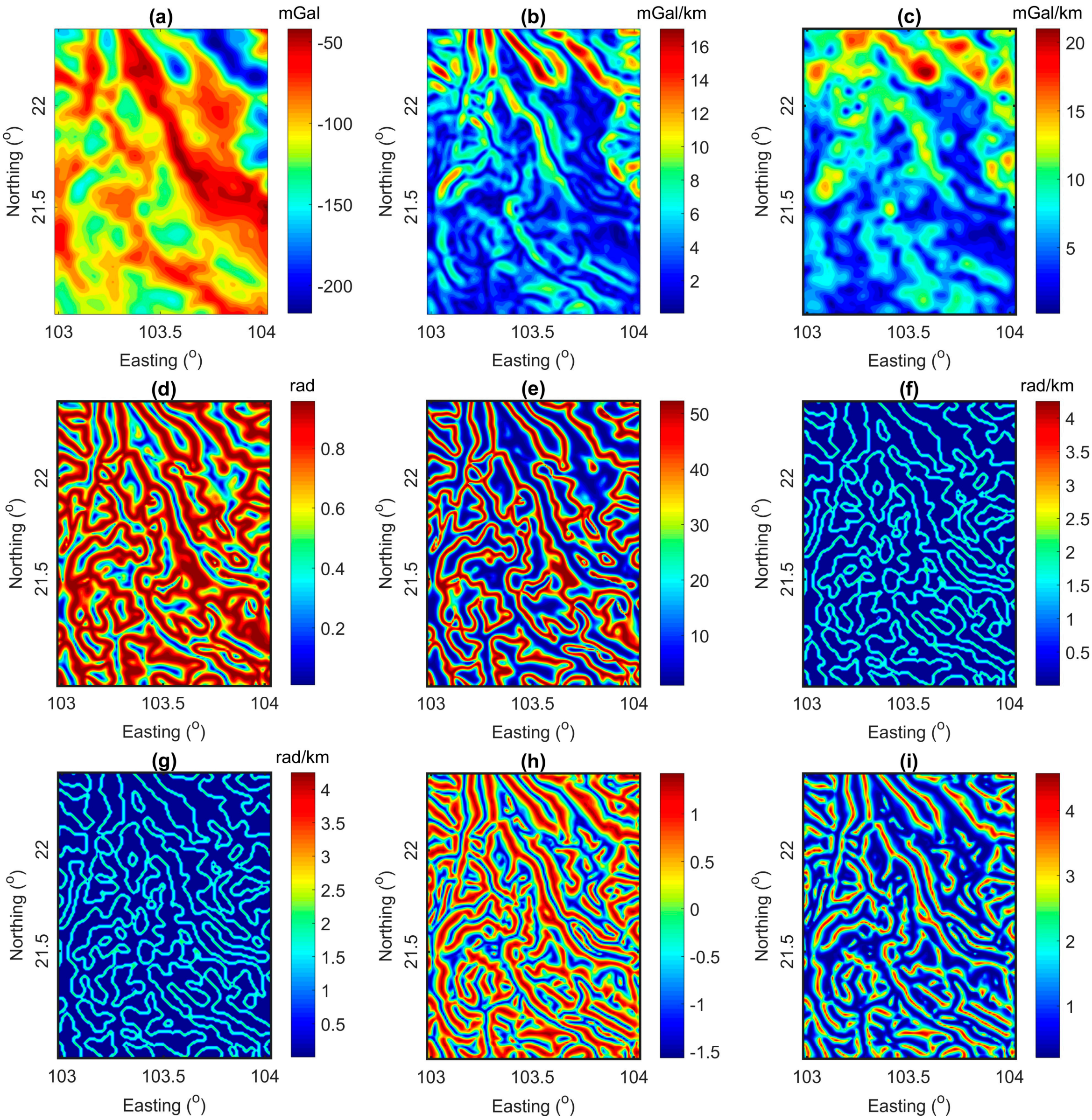

Figure 10. (**a**) Bouguer data of the Tuan Giao. (**b**) *HG*. (**c**) *AS*. (**d**) TM. (**e**) *ETM* with $p = 4$. (**f**) *HGNTilt*. (**g**) *HGimpTDX*. (**h**) *TAHG*. (**i**) *ETAHG* with $p = 1$.

5. Conclusions

In this paper, we have presented an improved method to extract the edges of gravity data. The method uses the exponential transform of the tilt angle of the horizontal gradient to enhance the edges. The theoretical tests show that the presented method can extract the edges of shallow and deep bodies simultaneously. In addition, this method produces results with more precise and clear boundaries compared to other methods. The application of the presented method is illustrated in mapping structures of the Tuan Giao (Vietnam) and boundaries of the Voisey's Bay Ni-Cu-Co deposit (Canada). The findings from the real examples are in agreement with the known structures of the study areas. Assuming that the magnetization direction is known, we can compute RTP magnetic data. Then, the presented method can be used for interpreting magnetic data.

Author Contributions: Conceptualization, L.T.P.; methodology, L.T.P. and S.P.O.; software, L.T.P. and S.P.O.; validation, N.T.B., A.H.V. and D.A.N.; investigation, L.T.P., S.P.O., C.V.A.L., N.T.B., A.H.V. and D.A.N.; data curation, N.T.B., A.H.V. and D.A.N.; writing—original draft preparation, L.T.P., S.P.O., C.V.A.L. and D.A.N.; writing—review and editing, L.T.P., S.P.O., C.V.A.L., N.T.B., A.H.V. and D.A.N.; supervision, C.V.A.L., S.P.O. and D.A.N. All authors have read and agreed to the published version of the manuscript.

Funding: This research was funded by PAS-VAST, QTPL01.01/22-23; and CNPq, 316376/2021-3.

Data Availability Statement: The data presented in this study are available on reasonable request from the corresponding author.

Acknowledgments: Authors thank for the result discussion of Phan Trong Trinh and the support of the senior researcher, NVCC 11.01/22-23. The authors thank two anonymous reviewers for their constructive comments.

Conflicts of Interest: The authors declare no conflict of interest.

References

1. Ai, H.; Ekinci, Y.L.; Balkaya, Ç.; Essa, K.S. Inversion of geomagnetic anomalies caused by ore masses using Hunger Games Search algorithm. *Earth Space Sci.* **2023**, *10*, e2023EA003002. [CrossRef]
2. Sampietro, D.; Capponi, M.; Maurizio, G. 3D Bayesian inversion of potential fields: The Quebec Oka carbonatite complex case study. *Geosciences* **2022**, *12*, 382. [CrossRef]
3. Boszczuk, P.; Cheng, L.Z.; Hammouche, H.; Roy, P.; Lacroix, S.; Cheilletz, A. A 3D gravity data interpretation of the Matagami mining camp, Abitibi Subprovince, Superior Province, Québec, Canada: Application to VMS deposit exploration. *J. Appl. Geophys.* **2011**, *75*, 77–86. [CrossRef]
4. Wijanarko, E.; Arisbaya, I.; Sumintadireja, P.; Grandis, H. Magnetotellurics study of Atambua area, West Timor, Indonesia. *Vietnam J. Earth Sci.* **2022**, *45*, 67–81. [CrossRef] [PubMed]
5. Xayavong, V.; Duc, M.V.; Singsoupho, S.; Anh, D.N.; Prasad, K.N.D.; Minh, T.V.; Do Anh, C. Combination of 2D-Electrical Resistivity Imaging and Seismic Refraction Tomography methods for groundwater potential assessments: A case study of Khammouane province, Laos. *Vietnam J. Earth Sci.* **2023**, *45*, 238–250. [CrossRef] [PubMed]
6. Marques, F.; Matos, J.X.; Sousa, P.; Represas, P.; Araujo, A.; Carvalho, J.; Morais, I.; Pacheco, N.; Albardeiro, L.; Goncalves, P. The role of land gravity data in the Neves-Corvo mine discovery and its use in present-day exploration and new target generation. *First Break* **2019**, *37*, 97–102. [CrossRef]
7. Nabighian, M.N.; Ander, M.E.; Grauch, V.J.S.; Hansen, R.O.; LaFehr, T.R.; Li, Y.; Pearson, W.C.; Peirce, J.W.; Phillips, J.D.; Ruder, M.E. Historical development of the gravity method in exploration. *Geophysics* **2005**, *70*, 63–89. [CrossRef]
8. Hinze, W.; Frese, R.; Saad, A. *Gravity and Magnetic Exploration: Principles, Practices, and Applications*; Cambridge University Press: Cambridge, UK, 2013.
9. Narayan, S.; Kumar, U.; Pal, S.K.; Sahoo, S.D. New insights into the structural and tectonic settings of the Bay of Bengal using high-resolution earth gravity model data. *Acta Geophys.* **2021**, *69*, 2011–2033. [CrossRef]
10. Narayan, S.; Sahoo, S.D.; Pal, S.K.; Kumar, U. Comparative evaluation of five global gravity models over a part of the Bay of Bengal. *Adv. Space Res.* **2022**, *71*, 2416–2436. [CrossRef]
11. Oksum, E. Grav3CH_inv: A GUI-based MATLAB code for estimating the 3-D basement depth structure of sedimentary basins with vertical and horizontal density variation. *Comput. Geosci.* **2021**, *155*, 104856. [CrossRef]
12. Kamto, P.G.; Oksum, E.; Pham, L.T.; Kamguia, J. Contribution of advanced edge detection filters for the structural mapping of the Douala Sedimentary Basin along the Gulf of Guinea. *Vietnam J. Earth Sci.* **2023**, *45*, 287–302.
13. Narayan, S.; Sahoo, S.D.; Pal, S.K.; Kumar, U.; Pathak, V.K.; Majumdar, T.J.; Chouhan, A. Delineation of structural features over a part of the Bay of Bengal using total and balanced horizontal derivative techniques. *Geocarto Int.* **2016**, *32*, 351–366. [CrossRef]

14. Ekinci, Y.L.; Yigitbas, E. Interpretation of gravity anomalies to delineate some structural features of Biga and Gelibolu peninsulas, and their surroundings (north-west Turkey). *Geodin. Acta* **2015**, *27*, 300–319. [CrossRef]
15. Eldosouky, A.M.; El-Qassas, R.A.Y.; Pham, L.T.; Abdelrahman, K.; Alhumimidi, M.S.; El Bahrawy, A.; Mickus, K.; Sehsah, H. Mapping Main Structures and Related Mineralization of the Arabian Shield (Saudi Arabia) Using Sharp Edge Detector of Transformed Gravity Data. *Minerals* **2022**, *12*, 71. [CrossRef]
16. Melouah, O.; Ebong, E.D.; Abdelrahman, K.; Eldosouky, A.M. Lithospheric structural dynamics and geothermal modeling of the Western Arabian Shield. *Sci. Rep.* **2023**, *13*, 11764. [CrossRef] [PubMed]
17. Kumar, U.; Pal, S.K.; Sahoo, S.D.; Narayan, S.; Saurabh, M.S.; Ganguli, S.S. Lineament mapping over Sir Creek offshore and its surroundings using high resolution EGM2008 gravity data: An integrated derivative approach. *J. Geol. Soc. India* **2018**, *91*, 671–678. [CrossRef]
18. Melouah, O.; Eldosouky, A.M.; Ebong, W.D. Crustal architecture, heat transfer modes and geothermal energy potentials of the Algerian Triassic provinces. *Geothermics* **2021**, *96*, 102211. [CrossRef]
19. Prasad, K.N.D.; Pham, L.T.; Singh, A.P. A novel filter "ImpTAHG" for edge detection and a case study from Cambay Rift Basin, India. *Pure Appl. Geophys.* **2022**, *179*, 2351–2364. [CrossRef]
20. Cooper, G.R.J. Novel Second-Order Derivative-Based Filters for Edge and Ridge/Valley Detection in Geophysical Data. *Minerals* **2023**, *13*, 1229. [CrossRef]
21. Cooper, G.R.J. Amplitude-Balanced Edge Detection Filters for Potential Field Data. *Explor. Geophys.* **2023**, *54*, 544–552. [CrossRef]
22. Kafadar, Ö. Applications of the Kuwahara and Gaussian filters on potential field data. *J. Appl. Geophys.* **2022**, *198*, 104583. [CrossRef]
23. Ekinci, Y.L.; Yiğitbaş, E. A geophysical approach to the igneous rocks in the Biga Peninsula (NW Turkey) based on airborne magnetic anomalies: Geological implications. *Geodin. Acta* **2012**, *25*, 267–285. [CrossRef]
24. Sahoo, S.D.; Narayan, S.; Pal, S.K. Fractal analysis of lineaments using CryoSat-2 and Jason-1 satellite-derived gravity data: Evidence of a uniform tectonic activity over the middle part of the Central Indian Ridge. *Phys. Chem. Earth* **2022**, *128*, 103237. [CrossRef]
25. Yuan, Y.; Yu, Q. Edge detection in potential-field gradient tensor data by use of improved horizontal analytic signal methods. *Pure Appl. Geophys.* **2015**, *172*, 461–472. [CrossRef]
26. Eldosouky, A.M.; Mohamed, H. Edge detection of aeromagnetic data as effective tools for structural imaging at Shilman area, South Eastern Desert, Egypt. *Arab. J. Geosci.* **2021**, *14*, 1–10. [CrossRef]
27. Eldosouky, A.M.; Pham, L.T.; Duong, V.H.; Ghomsi, F.E.K.; Henaish, A. Structural interpretation of potential field data using the enhancement techniques: A case study. *Geocarto Int.* **2022**, *37*, 16900–16925. [CrossRef]
28. Cordell, L. Gravimetric expression of graben faulting in Santa Fe Country and the Espanola Basin. In *30th Field Conference, Socorro, NM, USA, 4–6 October 1979: New Mexico Geological Society Guidebook*; New Mexico Geological Society: Socorro, NM, USA, 1979; pp. 59–64.
29. Roest, W.R.; Verhoef, J.; Pilkington, M. Magnetic interpretation using the 3-D analytic signal. *Geophysics* **1992**, *57*, 116–125. [CrossRef]
30. Fedi, M.; Florio, G. Detection of potential fields source boundaries by enhanced horizontal derivative method. *Geophys. Prospect.* **2001**, *49*, 40–58. [CrossRef]
31. Beiki, M. Analytic signals of gravity gradient tensor and their application to estimate source location. *Geophysics* **2010**, *75*, 159–174. [CrossRef]
32. Alvandi, A.; Ardestani, V.E. Edge detection of potential field anomalies using the Gompertz function as a high-resolution edge enhancement filter. *Bull. Geophys. Oceanogr.* **2023**, *64*, 279–300.
33. Miller, H.G.; Singh, V. Potential field tilt a new concept for location of potential field sources. *J. Appl. Geophys.* **1994**, *32*, 213–217. [CrossRef]
34. Wijns, C.; Perez, C.; Kowalczyk, P. Theta map: Edge detection in magnetic data. *Geophysics* **2005**, *70*, 39–43. [CrossRef]
35. Li, L. Improved edge detection tools in the interpretation of potential field data. *Explor. Geophys.* **2013**, *44*, 128–132. [CrossRef]
36. Cooper, G.; Cowan, D. Enhancing potential field data using filters based on the local phase. *Comput. Geosci.* **2006**, *32*, 1585–1591. [CrossRef]
37. Ferreira, F.J.F.; de Souza, J.; Bongiolo, A.B.S.; de Castro, L.G. Enhancement of the total horizontal gradient of magnetic anomalies using the tilt angle. *Geophysics* **2013**, *78*, 33–41. [CrossRef]
38. Yuan, Y.; Gao, J.Y.; Chen, L.N. Advantages of horizontal directional Theta method to detect the edges of full tensor gravity gradient data. *J. Appl. Geophys.* **2016**, *130*, 53–61. [CrossRef]
39. Nasuti, Y.; Nasuti, A.N. Tilt as an improved enhanced tilt derivative filter for edge detection of potential field anomalies. *Geophys. J. Int.* **2018**, *214*, 36–45. [CrossRef]
40. Zareie, V.; Moghadam, R.H. The application of theta method to potential field gradient tensor data for edge detection of complex geological structures. *Pure Appl. Geophys.* **2019**, *176*, 4983–5001. [CrossRef]
41. Pham, L.T.; Oksum, E.; Do, T.D. Edge enhancement of potential field data using the logistic function and the total horizontal gradient. *Acta Geod. Geophys.* **2019**, *54*, 143–155. [CrossRef]
42. Pham, L.T.; Vu, T.V.; Le, T.S.; Trinh, P.T. Enhancement of potential field source boundaries using an improved logistic filter. *Pure Appl. Geophys.* **2020**, *177*, 5237–5249. [CrossRef]

43. Pham, L.T.; Eldosouky, A.M.; Oksum, E.; Saada, S.A. A new high resolution filter for source edge detection of potential field data. *Geocarto Int.* **2022**, *37*, 3051–3068. [CrossRef]
44. Ibraheem, I.M.; Tezkan, B.; Ghazala, H.; Othman, A.A. A New Edge Enhancement Filter for the Interpretation of Magnetic Field Data. *Pure Appl. Geophys.* **2023**, *180*, 2223–2240. [CrossRef]
45. Ekinci, Y.L.; Ertekin, C.; Yigitbas, E. On the effectiveness of directional derivative based filters on gravity anomalies for source edge approximation: Synthetic simulations and a case study from the Aegean graben system (western Anatolia, Turkey). *J. Geophys. Eng.* **2013**, *10*, 035005. [CrossRef]
46. Pham, L.T.; Oksum, E.; Kafadar, O.; Trinh, P.T.; Nguyen, D.V.; Vo, Q.T.; Le, S.T.; Do, T.D. Determination of subsurface lineaments in the Hoang Sa islands using enhanced methods of gravity total horizontal gradient. *Vietnam J. Earth Sci.* **2022**, *44*, 395–409.
47. Nasuti, Y.; Nasuti, A.; Moghadas, D. STDR: A novel approach for enhancing and edge detection of potential field data. *Pure Appl. Geophys.* **2019**, *176*, 827–841. [CrossRef]
48. Liu, J.; Li, S.; Jiang, S.; Wang, X.; Zhang, J. Tools for Edge Detection of Gravity Data: Comparison and Application to Tectonic Boundary Mapping in the Molucca Sea. *Surv. Geophys.* **2023**, *44*, 1781–1810. [CrossRef]
49. Farquharson, C.G.; Ash, M.R.; Miller, H.G. Geologically constrained gravity inversion for the Voisey's Bay ovoid deposit. *Lead. Edge* **2008**, *27*, 64–69. [CrossRef]
50. Li, C.; Naldrett, A. Geology and petrology of the Voisey's Bay intrusion: Reaction of olivine with sulfide and silicate liquids. *Lithos* **1999**, *47*, 1–31. [CrossRef]
51. Ryan, B. *Geological Map of the Nain Plutonic Suite and Surrounding Rocks Nain-Nutak, NTS 14SW. Geological Survey Branch, Newfoundland Department of Mines and Energy, Scale 1:500,000*; Government of Newfoundland and Labrador: St. John's, NL, Canada, 1990.
52. King, A. Review of Geophysical Technology for Ni-Cu-PGE deposits. In Proceedings of the Exploration 07: Fifth Decennial International Conference on Mineral Exploration, Toronto, ON, Canada, 9–12 September 2007; Milkereit, B., Ed.; CVRD Exploration Canada Inc.: Cliff, ON, Canada, 2007; pp. 647–665.
53. Lelièvre, P.; Carter-McAuslan, A.; Farquharson, C.; Hurich, C. Unified geophysical and geological 3D Earth models. *Lead. Edge* **2012**, *31*, 322–328. [CrossRef]
54. Duong, N.A.; Sagiya, T.; Kimata, F.; Tran, D.T.; Vy, Q.H.; Cong, D.C.; Binh, N.X.; Xuyen, N.D. Contemporary horizontal crustal movement estimation for northwestern Vietnam inferred from repeated GPS measurements. *Earth Planets Space* **2013**, *65*, 1399–1410. [CrossRef]
55. Zhou, M.F.; Chen, W.T.; Wang, C.Y.; Prevec, S.A.; Liu, P.P.; Howarth, G.H. Two stages of immiscible liquid separation in the formation of Panzhihua-type Fe–Ti–V oxide deposits, SW China. *Geosci. Front.* **2013**, *4*, 481–502. [CrossRef]
56. Roger, F.; Maluski, H.; Lepvrier, C.; Van, T.V.; Paquette, J.-L. LA-ICPMS zircons U/Pb dating of Permo-Triassic and Cretaceous magmatisms in Northern Vietnam–Geodynamical implications. *J. Asian Earth Sci.* **2012**, *48*, 72–82. [CrossRef]
57. Tran, T.A.; Tran-Trong, H.; Pham-Ngoc, C.; Shellnutt, J.G.; Pham, T.T.; Izokh, A.E.; Pham, P.L.T.; Duangpaseuth, S.; Soulintone, O. Petrology of the Permian-Triassic granitoids in Northwest Vietnam and their relation to the amalgamation of the Indochina and Sino-Vietnam composite terranes. *Vietnam J. Earth Sci.* **2022**, *44*, 343–368. [CrossRef] [PubMed]
58. Pham, L.T. A comparative study on different methods for calculating gravity effect of an uneven layer: Application to computation of Bouguer gravity anomaly in the East Vietnam Sea and adjacent areas. *VNU J. Sci. Math Phys.* **2020**, *36*, 106–114.